Radiochemical synthesis and evaluation in nonhuman primates of 3-[11C]methoxy-4-aminopyridine: a novel PET tracer for Imaging Potassium Channels in the CNS

Nicolas J. Guehl[1,#], **Ramesh Neelamegam**[1,2,#], **Yu-Peng Zhou**[1,#], **Sung-Hyun Moon**[1], **Maeva Dhaynaut**[1], **Georges El Fakhri**[1], **Marc D. Normandin**[1,*], **Pedro Brugarolas**[1,*]

[1]Gordon Center for Medical Imaging, Department of Radiology, Massachusetts General Hospital and Harvard Medical School, Boston, MA

[2]Present address: Department of Radiology, The University of Texas Health Science at San Antonio, San Antonio, Texas, TX

Abstract

Demyelination, the loss of the protecting sheath of neurons, contributes to disability in many neurological diseases. In order to fully understand its role in different diseases and to monitor treatments aiming at reversing this process, it would be valuable to have PET radiotracers that can detect and quantify molecular changes involved in demyelination. Carbon-11 labeled radiotracers present the advantage of allowing for multiple scans on the same subject in the same day. Here, we describe [11C]3MeO4AP, a novel ^{11}C-labeled version of the K^+ channel tracer [18F]3F4AP, and characterize its imaging properties in two nonhuman primates including a monkey with a focal brain injury sustained during a surgical procedure three years prior to imaging. Our findings show that [11C]3MeO4AP is brain permeable, metabolically stable and has high plasma availability. When compared with [18F]3F4AP, [11C]3MeO4AP shows very high correlation in volumes of distribution (V_T) confirming a common target. [11C]3MeO4AP shows slower washout than [18F]3F4AP suggesting stronger binding. Finally, similar to [18F]3F4AP, [11C]3MeO4AP is highly sensitive to the focal brain injury. All these features make it a promising radioligand for imaging demyelinated lesions.

Keywords

Demyelination; K^+ channels; PET; carbon-11; radiochemistry; pharmacokinetics

Introduction

Demyelination –the loss of the insulating sheath that surrounds axons– is a major contributor to disability in multiple sclerosis (MS)[1] and likely in other diseases such as stroke[2], traumatic brain and spinal cord injuries[3,4] and Alzheimer's disease[5]. In order to understand the role of demyelination in different neurological diseases and to be able to monitor therapies aiming to promote remyelination, it is critical to develop noninvasive imaging tools that are sensitive to demyelination[6,7].

To that end, we previously described [^{18}F]3F4AP, a radiofluorinated analog of the multiple sclerosis drug 4-aminopyridine (4AP), as a promising radioligand for imaging demyelination[8-10]. [^{18}F]3F4AP binds to axonal voltage-gated K$^+$ (K$_v$) channels, which increase in expression and become more accessible after demyelination[11-15]. Given the significant changes in K$^+$ channels with demyelination, we previously hypothesized that [^{18}F]3F4AP could be used to detect demyelinated lesions using positron emission tomography (PET) and, subsequently, confirmed this experimentally in rodent models of demyelination[8]. More recently, we evaluated [^{18}F]3F4AP in nonhuman primates (NHPs) and demonstrated that it has favorable imaging properties and is sensitive to a focal brain injury[16].

While ^{18}F-labeled tracers ($t_{1/2}$ = 110 min) can be produced remotely and distributed regionally, there are instances where having a shorter-lived radiotracer can be advantageous. For example, ^{11}C-labeled tracers ($t_{1/2}$ = 20.4 min) allow performing two scans on the same subject in the same day, which facilitates the assessment of test/retest variability, conducting paired baseline-blocking studies, comparing two radiotracers, or acquiring data with two complementary radiotracers. Furthermore, developing different ^{18}F- and ^{11}C-labeled analogs of a given compound provides the opportunity to perform structure-activity relationship studies, which can potentially result in the identification of radioligands with improved physicochemical properties. Thus, in a recent work, we investigated four novel derivatives of 4AP as potential candidates for PET imaging of demyelination[17]. Among those, 3-methoxy-4-aminopyridine (3MeO4AP) was found to bind to Shaker K$_v$ channel with similar affinity as 4AP and 3F4AP and demonstrated favorable physicochemical properties. Its pK_a value was found to be 9.18 indicating that at physiological pH this compound is mostly in its protonated form, the required form for binding to the channel. In terms of lipophilicity, 3MeO4AP was found to have an octanol/water partition coefficient at pH 7.4 (logD) of −0.76 suggesting that it may penetrate the blood-brain barrier (BBB) faster than 4AP (logD = −1.48) but slower than 3F4AP (logD = 0.41). Taken together, these *in vitro* results suggest that 3MeO4AP is a promising candidate for PET imaging.

In the present work, we present the novel ^{11}C-labeled radiotracer 3-[^{11}C]methoxy-4-aminopyridine, [^{11}C]3MeO4AP, and its evaluation in NHPs. Specifically, we describe its radiochemical synthesis via [^{11}C]methylation, its characterization in NHPs including pharmacokinetic modeling with arterial input functions, and the direct comparison with [^{18}F]3F4AP using a graphical method previously reported by Guo et al[18].

Results and Discussion

3-[¹¹C]methoxy-4-aminopyridine synthesis by direct ¹¹C-methylation

Radiochemical synthesis of [¹¹C]3MeO4AP (**2**) was accomplished via [¹¹C]methylation of 3-hydroxy-4-aminopyridine (**1**) with [¹¹C]methyl iodide in DMSO at 80 °C under basic conditions (Figure 1A). A summary of the conditions tested are shown in Sup. Table 1. Using this method, 3-[¹¹C]methoxy-4-aminopyridine (**2**) was produced with high molar activity (1.4 ± 0.1 Ci/µmol), high radiochemical purity (> 98.5%) and $15 \pm 4\%$ ($n = 6$) non-decay corrected radiochemical yield (Figure 1B and C). The total time from end of bombardment to reformulation was *ca.* 40 min.

[¹¹C]3MeO4AP in nonhuman primates: Analysis of arterial blood

Immediately after producing [¹¹C]3MeO4AP, the radiotracer was administered intravenously as a 3 min slow bolus to nonhuman primates (NHPs) positioned inside a PET/CT scanner. During the scan, serial arterial samples were collected and analyzed for radioactivity concentration in whole-blood (WB) and plasma (PL), radiometabolites and plasma free fraction (f_p). Total radioactivity in WB and PL peaked quickly and cleared rapidly after the 3 min venous infusion of [¹¹C]3MeO4AP (Figure 2A and B). The ratio of WB to PL concentration reached equilibrium within 1 min and was close to unity (WB:PL at 1-min post-injection across all studies = 1.21 ± 0.04). RadioHPLC metabolite measurements showed minimal metabolic degradation with $86.2 \pm 4.6\%$ parent remaining after 60 min post injection (Figure 2C and Supplemental Figure 1). Finally, f_p measurements showed minimal binding to plasma proteins ($f_p = 100\%$ in Monkey 1 and 96% in Monkey 2, measured in triplicate for n = 1 imaging experiment per monkey).

[¹¹C]3MeO4AP in nonhuman primates: Brain uptake and pharmacokinetic modeling

[¹¹C]3MeO4AP entered the brain readily and peaked relatively quickly. 20 min post-injection the standardized uptake value (SUV) in gray matter areas was greater than 2 and around 1.5 in white matter. Uptake and kinetics were relatively heterogeneous across brain regions. Figure 3A shows the time activity curves (TACs) from baseline studies acquired in each monkey and Figure 3B the SUV images calculated from 45 to 90 min post tracer injection (SUV$_{45-90min}$).

Visually, brain TACs were well described by both reversible one tissue (1T) and two tissue (2T) compartment models for the entire 120 min of scan acquisition. However, in this work 90 min of data was used as the reference scan duration for the kinetic analyses because of increased statistical noise in late PET images as well as in the parent fraction measurements. According to the Akaike information criterion (AIC)[19], over all TACs and studies the preferred model was a reversible 1T model with the vascular contribution v included as a model parameter (1T2k1v) (AIC$_{weight,median}$ = 0.339), followed by a reversible 2T model with the vascular contribution v included as a model parameter (2T4k1v) (AIC$_{weight,median}$ = 0.128). V_T values estimated from the 1T2k1v and 2T4k1v models were stable and in very good agreement ($V_{T,2T4k1v}$ = 0.99 x $V_{T,1T2k1v}$ + 0.08; r = 0.99, $p < 0.0001$; mean difference = 0.03 ± 0.1 mL/cc, average measure intraclass correlation coefficient ICC = 0.996 with CI95% of [0.993, 0.998]). Since the 1T2k1v model adequately described the kinetics of

[^{11}C]3MeO4AP (Figure 3A) and the more complex 2T4k1v model was not statistically justified, we chose the 1T2k1v model to quantify [^{11}C]3MeO4AP signal. The quantitative analysis confirmed the good brain penetration of the radiotracer with an average K_I value of 0.16 ± 0.01 mL/min/cc for the whole brain, as measured across all studies. Figure 3C shows bar plots of the average V_T values of baseline scans for each animal. The lowest V_T value was measured in the white matter and V_T measurements were higher in cortical areas. The highest V_T was found in the amygdala. Test-retest (TRT) was excellent in Monkey 2 (mean TRT = $1.0 \pm 3.6\%$ across brain regions, average measure ICC = 0.976 with CI95% of [0.908, 0.994]) and so was the reproducibility of V_T measurements for the two baseline scans acquired in Monkey 1 three months apart (mean difference = $3.9 \pm 3.3\%$ across brain regions, average measure ICC = 0.978 with CI95% of [0.722, 0.996]). Across all baseline studies and brain regions, the average coefficient of variation (COV) was $5.6 \pm 3.3\%$, with the lowest COV measured in the white matter (2.4%) and highest COV measured in the striatum (11.7%). Table 1 shows V_T values obtained for all studies. Coadministration of [^{11}C]3MeO4AP and nonradioactive 3MeO4AP (1.16 mg/kg) did not show a reduction in V_T, likely because the dose was below the pharmacological dose. These findings are consistent with previous studies with [^{18}F]3F4AP, which showed that administration of similar doses of 3F4AP did not cause a reduction in V_T likely due to a compensatory mechanism by which when some channels become occupied others transition to the open and bindable conformation[16]. We did not attempt coadministration of higher doses of nonradioactive 3MeO4AP as previous studies have shown that high doses of 4AP and related compounds can cause seizures[8,20].

V_T estimates were stable when truncating the data down to 60 min. V_T values obtained using only 60 min of data were in excellent agreement with those obtained using 90 min of data (mean difference = 0.007 ± 0.224 mL/cc, average measure ICC = 0.984 with CI95% of [0.972,0.991]). Likewise, and despite the increased statistical noise in the measurements late in the scan, V_T estimates obtained when using 120 min of data were in excellent agreement with those obtained using 90 min of data (mean difference = 0.000 ± 0.125 mL/cc, average measure ICC = 0.994 with CI95% of [0.989,0.997]).

Logan plots linearized very well by a t^* of 10 min and resulted in estimates of V_T that were highly correlated with those obtained from the 1T2k1v model despite some small underestimation ($V_{T,Logan} = 0.91$ x $V_{T,1T2k1v} + 0.27$; $r = 0.99$, $p < 0.0001$; mean difference = -0.22 ± 0.10 mL/cc, average measure ICC = 0.977 with CI95% of [0.149,0.995]). Figure 4 shows Logan plots as well as parametric maps of V_T obtained for each animal. Similar to the observation made for the Logan graphical method, using a t^* of 10 min the multilinear analysis 1 (MA1) regression model demonstrated good agreement with the full compartmental analysis with a small underestimation ($V_{T,MA1} = 0.96$ x $V_{T,1T2k1v} + 0.06$; $r = 0.99$, $p<0.0001$; mean difference = -0.19 ± 0.09 mL/cc, average measure ICC = 0.984 with CI95% of [0.223,0.996]).

[^{11}C]3MeO4AP in nonhuman primates: Sensitivity to a focal traumatic brain injury

One of the monkeys we imaged had sustained a minor intracranial injury during a craniotomy procedure three years prior to imaging. The location of the craniotomy site can

be clearly seen on the CT images (Figure 5A top). PET images of the region of the brain right under the burr hole on the skull showed a marked increase in [^{11}C]3MeO4AP signal (Figure 5A bottom). Quantitative analysis showed a 60.3% increase in V_T in this region compared to the contralateral side (V_T lesion = 7.29 mL/cc, V_T contra = 4.55 mL/cc; TRT = 0.9%, n = 2) and slower kinetics (Figure 5B). This change could not be attributed to increase in perfusion as the 1T2k1v model actually showed a decrease in K_1 (−38.7% on average between the two baseline scans) in this region compared to the contralateral side. Despite the slower kinetics in the lesion, V_T estimates were relatively stable when truncating the acquisition down to 60 min with differences in V_T within 10% when compared to 90 min of data.

Direct comparison between [^{11}C]3MeO4AP and [^{18}F]3F4AP using a graphical method

We recently reported the pharmacokinetic evaluation of [^{18}F]3F4AP in the same two animals[16]. Compared to [^{18}F]3F4AP, [^{11}C]3MeO4AP displayed more heterogeneity across brain regions and slower kinetics. The rank order of V_T values across brain regions was largely consistent between the two tracers. Direct comparison of the regional V_T values of [^{11}C]3MeO4AP and [^{18}F]3F4AP in both animals showed a strong linear relationship (Figure 6A: r = 0.97, p<0.0001 for Monkey 1; Figure 6B: r = 0.85, p=0.0017 for Monkey 2; Figure 6C: r = 0.93, p<0.0001 for Monkey 1 and 2 combined on the same plot) indicating that the two ligands bind to a common target. The linear regressions showed negative y-intercepts (Figure 6A: y = −1.63, p=0.0312 for Monkey 1; Figure 6B: y = −0.58, p=0.6693 for Monkey 2; Figure 6C: y = −1.27, p=0.0561 for both animals combined) suggesting that [^{11}C]3MeO4AP has higher specific binding than [^{18}F]3F4AP ($BP_{ND}^{[11C]3MeO4AP} > BP_{ND}^{[18F]3F4AP}$). After swapping the axes of plots in Figure 6, y-intercept of all plots became positive (y = 0.62, p = 0.0031 for Monkey 1; y = 0.78, p=0.0444 for Monkey 2; y = 0.67, p=0.0003 for both animals combined, graphs not shown) thus preserving the rank order of $BP_{ND}^{[11C]3MeO4AP}$ and $BP_{ND}^{[18F]3F4AP}$. This result indicates that the determination of the rank order of BP_{ND} between [^{11}C]3MeO4AP and [^{18}F]3F4AP from the y-intercept is not affected to a significant level by noise on the axis[18], as standard linear regression assumes that data plotted on the x-axis is noiseless. Lastly, we estimated the *in vivo* K_D ratio between [^{11}C]3MeO4AP and [^{18}F]3F4AP using the f_p measurements of both tracers. The *in vivo* affinity ratios $K_D^{[18F]3F4AP} / K_D^{[11C]3MeO4AP}$ were 2.82 for Monkey 1 (Figure 6A), 2.58 for Monkey 2 (Figure 6B) and 2.78 when combining Monkey 1 and 2 on the same graph (Figure 6C), thus suggesting that [^{11}C]3MeO4AP has higher *in vivo* affinity than [^{18}F]3F4AP for K_v channels.

Summary and discussion

Demyelination is emerging as an important pathological feature in many neurological diseases in addition to multiple sclerosis. These include traumatic brain and spinal cord injuries, stroke, dementias and psychiatric disorders. Given the lipophilic nature of the myelin sheath, demyelinated lesions are usually detectable on MRI. However, there are some limitations for imaging demyelination using MR sequences, including a lack of specificity[22], the difficulty of detecting grey matter lesions where myelin is discontinuous and sparse[23]

and the challenge of obtaining quantitative measurements[24]. Given these limitations, the use of PET radioligands that target proteins differentially expressed in demyelinated lesions appears to be a highly promising approach[6]. To that end, we previously developed [^{18}F]3F4AP (a radiofluorinated analog of the multiple sclerosis drug 4-aminoyridine) as an ^{18}F-labeled PET ligand for voltage-gated potassium channels ($K_v1.1$ and $K_v1.2$)[8]. $K_v1.1$ and $K_v1.2$ are a relevant target as these channels significantly increase in expression and in accessibility upon demyelination[12,13,25]. In our previous work, we showed that [^{18}F]3F4AP can detect demyelinated lesions in rodent models of MS[8] and, more recently, that it has favorable pharmacokinetic properties in non-human primates and is highly sensitive to a focal brain injury[16]. In a parallel but related effort, we also investigated four novel derivatives of 4AP as potential candidates for imaging and/or therapy, among which 3MeO4AP was found to possess good binding affinity as well as suitable basicity (essential for binding) and lipophilicity (essential for brain penetration)[17].

In the present work, we described the radiochemical synthesis of [^{11}C]3MeO4AP via standard ^{11}C-methylation using [^{11}C]methyl iodide (Figure 1). Subsequent imaging studies in NHPs showed suitable pharmacokinetics both in plasma and in brain. Analyses of arterial plasma samples demonstrated a high metabolic stability, minimal plasma protein binding, and relatively rapid plasma clearance (Figure 2). [^{11}C]3MeO4AP readily entered the monkey brain and showed relatively heterogenous uptake and kinetics across brain regions (Figure 3). Highest uptake was seen in the amygdala and lowest in the white matter. A 1-tissue compartment model with the vascular contribution v included as a model parameter (1T2k1v) was found to be sufficient to describe the brain time activity curves in all brain regions and provided robust estimates of the total volume of distribution (V_T) (Figure 4). Test-retest performed on the same day in Monkey 2 was excellent and so was the reproducibility of V_T estimates for the two baseline scans acquired in Monkey 1, thus demonstrating the basic reproducibility of [^{11}C]3MeO4AP quantitative measurements. Simplified methods such as the Logan and MA1 graphical methods provided V_T measurements that were in good agreement with those obtained from the full compartmental analysis. Similar to [^{18}F]3F4AP, [^{11}C]3MeO4AP was found to be highly sensitive to a focal traumatic injury that occurred 3 years prior to imaging (Figure 5).

When compared to [^{18}F]3F4AP, [^{11}C]3MeO4AP demonstrated slower brain penetration, which can be quantitatively assessed from the K_I estimates ($K_{I[11C]3MeO4AP} = 0.16 \pm 0.01$ mL/min/cc *vs.* $K_{I[18F]3F4AP} = 0.45 \pm 0.10$ mL/min/cc, measured in whole brain across baseline studies), followed by slower washout. The differences in brain penetration can be attributed to the lower lipophilicity of [^{11}C]3MeO4AP compared to [^{18}F]3F4AP (logD at pH 7.4 = −0.76 vs. 0.41). The slower washout is consistent with stronger binding of [^{11}C]3MeO4AP to K_v channels in the CNS. This was quantitatively assessed using the graphical analysis method developed by Guo et al[18]. The analysis showed a strong linear correlation in V_T values across all brain regions confirming that [^{18}F]3F4AP and [^{11}C]3MeO4AP bind to the same target (Figure 6). In addition, the f_p *values* measured for each tracer and the slope estimated from the linear regression suggested that [^{11}C]3MeO4AP has higher *in vivo* binding affinity than [^{18}F]3F4AP and the intercept suggested higher *in vivo* specific binding. The findings of greater affinity and specific binding are likely due to the higher pK_a of [^{11}C]3MeO4AP (9.1) compared [^{18}F]3F4AP (7.4), which indicates that at

physiological pH more of [^{11}C]3MeO4AP exists in the protonated form, required to bind to the K$^+$ channel[17].

In summary, this study demonstrates that [^{11}C]3MeO4AP is a promising tracer for imaging K$_v$ channels in the brain, which have been closely linked to changes in demyelination and remyelination. Given the shorter half-life of [^{11}C]3MeO4AP compared to [^{18}F]3F4AP, this tracer has the potential to offer a viable option when multiple studies on the same subject and the same day are required.

Materials and Methods

Compliance

All experiments involving nonhuman primates were performed in accordance with the U.S. Department of Agriculture (USDA) Animal Welfare Act and Animal Welfare Regulations (Animal Care Blue Book), Code of Federal Regulations (CFR), Title 9, Chapter 1, Subchapter A, Part 2, Subpart C, §2.31. 2017. Experiments were approved by the Animal Care and Use Committee at the Massachusetts General Hospital.

Radiochemistry

Materials: 4-amino-3-hydroxypyridine and 4-amino-3-methoxypyridine were purchased from Astatech (cat# 22383 and 35474). Anhydrous solvents were purchased from Acros Organics. All other chemicals were purchased from Sigma.

Radiochemical synthesis of [^{11}C]3MeO4AP: Supplemental table 1 shows a summary of the conditions tested during development. *Final method*: 4-amino-3-hydroxypyridine (**1**, 2 ± 0.5 mg) was dissolved in 0.3 mL of DMSO and 4 μL of 8 N NaOH added to it. [^{11}C]CH$_3$I (7.4-22.2 GBq) produced in the GE Tracerlab FX MeI was bubbled into the precursor solution, sealed and allowed to react at 80 °C for 3 minutes. The reaction mixture was diluted with 5 mL of water and purified using reverse-phase HPLC (Waters XBridge C18; 5 μm, 10x250 mm; 5% EtOH in 95% sodium phosphate (10 mM, pH = 8); Flow: 3 mL/min; R$_t$ ~9.3 min) or by Sep-pak purification. For Sep-pak purification the reaction mixture was diluted with 20 mL of water, loaded onto a C18 cartridge (Waters) eluted with 10% EtOH in saline. Molar activity, chemical and radiochemical purity were assessed by analytical HPLC (Waters XBridge C18; 3.5u, 4.6 x 100 mm; 5% MeCN in 95% ammonium bicarbonate (10 mM); Flow: 1 mL/min; R$_t$ ~5 min). Compound identity was confirmed by coinjection with authentic reference standard on HPLC.

Imaging studies

Animals: Two male adult rhesus macaques (Monkey 1 and Monkey 2) were used in this study (ages: 9 and 13 years old, respectively). Animal body weights on the day of imaging were 14.5 kg on average for Monkey 1 (range 14.3 - 14.6 kg) and 16.2 kg for Monkey 2. As previously reported, one of the animals (Monkey 2) had sustained an accidental injury during a craniotomy procedure three years prior imaging[16].

Animal preparation: Prior to each imaging session, animals were sedated with ketamine/ xylazine (10/0.5 mg/kg IM) and were intubated for maintenance anesthesia with isoflurane (1-2% in 100% O2). A venous catheter was placed in the saphenous vein for radiotracer injection and, an arterial catheter was placed in the posterior tibial artery for blood sampling. The animal was positioned on a heating pad on the bed of the scanner for the duration of the study.

Magnetic Resonance Imaging: *For each monkey,* a 3-dimensional structural T1-weighted magnetization-prepared rapid gradient-echo (MEMPRAGE) was acquired using a 3T Biograph mMR (Siemens Medical Systems) for anatomical reference. Acquisitions parameters were as follows: repetition time =2,530 ms; echo time =1.69 ms; inversion time =1100 ms; flip angle = 7; voxel size = 1x1x1 mm^3 and matrix size = 256 x 256 x 176, number of averages= 4.

Positron Emission Tomography Imaging: The two animals (Monkey 1 and Monkey 2) were scanned on a Discovery MI (GE Healthcare) PET/CT scanner. Each monkey underwent two baseline scans which were separated by 3 months for Monkey 1 and acquired on the same day for Monkey 2. Monkey 1 also had another scan with co-injection of unlabeled 3MeO4AP (1.16 mg/kg) which was acquired on the same day as one of the baseline scans. A CT scan was acquired prior each PET acquisition for attenuation correction. Emission PET data were acquired in 3D list mode for at least 120 min following injection of [^{11}C]3MeO4AP. Radiotracer and unlabeled 3MeO4AP were administered via the lateral saphenous vein over a 3-minute infusion and followed by a 3-minute infusion of saline flush. All injections were performed using syringe pumps (Medfusion 3500). The injected dose of [^{11}C]3MeO4AP at the time of injection was 292.0 ± 67.7 MBq (range 177.6 –352.8, n = 4). Molar activity (A_m) of [^{11}C]3MeO4AP at time of injection was 53.3 ± 4.1 GBq/µmol (n = 2) corresponding to injected masses of 636 ± 252 ng (n = 2). Dynamic PET data were reconstructed using a validated fully 3D time-of-flight iterative reconstruction algorithm using 3 iterations and 34 subsets while applying corrections for scatter, attenuation, deadtime, random coincident events, and scanner normalization. For all dynamic scans, list mode data were framed into dynamic series of 6x10, 8x15, 6x30, 8x60, 8x120s and remaining were 300-s frames. Final reconstructed images had voxel dimensions of 256 x 256 x 89 and voxel sizes of 1.17 x 1.17 x 2.8 mm^3.

Arterial blood sampling: Arterial blood sampling was performed during the course of the dynamic PET acquisitions. Samples of 1 to 3 mL were initially drawn every 30 seconds upon radiotracer injection and decreased in frequency to every 15 minutes toward the end of the scan. [^{11}C]3MeO4AP metabolism was characterized from blood samples acquired at 3, 5, 10, 15, 30, 60, 90, and up to 120 minutes. An additional blood sample of 3 mL was drawn prior tracer injection in order to measure the plasma free fraction f_p of [^{11}C]3MeO4AP (n = 1 for each monkey).

Arterial blood analysis: Radioactivity concentration (in kBq/cc) was measured in whole-blood (WB) and subsequently in plasma (PL) following the centrifugation of WB. Radiometabolite analysis was performed using an automated column switching radio-HPLC

(High Performance Liquid Chromatography) system[26,27]. Eluent was collected in 1-minute intervals and assayed for radioactivity using a Wallac Wizard gamma counter (1470 model). The procedure adopted for these measurements was similar to the one described in Guehl et al[16], except for the mobile phases used. Injected plasma samples were initially trapped on the catch column using a mobile phase consisting of either 99:1 10 mM ammonium bicarbonate pH 8 in water:MeCN or 99:1 10 mM ammonium phosphate pH 8 in water:EtOH at 1.8 mL/min and the catch column was backflushed with either 95:5 10 mM ammonium bicarbonate pH 8 in water:MeCN or 95:5 10 mM ammonium phosphate pH 8 in water:EtOH at 1 mL/min and the sample directed onto the analytical column. Standardized uptake value (SUV) radioactivity time courses in WB and in PL were generated by correcting radioactivity concentrations (C [kBq/ml]) for injected dose (ID [MBq]) and animal body weight (BW [kg]) and were calculated as $SUV(t) = C(t)/(ID/BW)$. Measured time courses of percent parent in plasma (%PP(t)) were fitted with a single exponential decay plus a constant and individual metabolite-corrected arterial input function were derived as previously described[16]. The plasma free fraction f_p of [11C]3MeO4AP was measured in triplicate by ultrafiltration following the procedure described in Guehl et al[16].

Image registration and processing: Structural MEMPRAGE and PET images were aligned into the MRI National Institute of Mental Health Macaque Template (NMT)[21] following the procedures extensively described in our previous work with [18F]3F4AP[16]. Time-activity curves (TACs) were extracted from the native PET image space for the occipital cortex, parietal cortex, temporal cortex, frontal cortex, hippocampus, amygdala, striatum, thalamus, white matter and whole cerebellum. In addition, the same region of interest (ROI) as in Guehl et al[12], manually drawn on the site of the intracranial lesion, was transposed to the native PET space for extraction of TACs.

Brain kinetic analysis: Extracted brain TACs were analyzed by compartmental modeling with reversible one-(1T) and two- (2T) tissue compartment models using the measured metabolite-corrected arterial plasma input function. Each model was assessed with the contribution of the WB radioactivity to the PET measurements. For quantification based on compartment models, we followed the consensus nomenclature for *in vivo* imaging of reversibly binding radioligands[28]. The primary outcome of interest was the total volume of distribution V_T representing the equilibrium ratio of tracer in tissue relative to plasma and which is linearly related to the tracer binding to the target. V_T was calculated as K_1/k_2 for a 1T compartment model and as $(K_1/k_2) \times (1 + k_3/k_4)$ for a 2T model. The optimal compartment model was chosen on the basis of the Akaike information criterion (AIC), visual assessment of the model fits as well as robustness of the V_T estimates. Graphical methods with arterial input functions, as alternative techniques for estimation of V_T, were also investigated and the Logan and multilinear analysis MA1 graphical methods[29,30] were tested. V_T parametric maps were generated using the Logan method.

Comparison between [11C]3MeO4AP and [18F]3F4AP by graphical method: In each animal, we performed a direct comparison of the *in vivo* specific binding of [11C]3MeO4AP and [18F]3F4AP using regional V_T values via linear regression, following the method described by Guo et al[18]. Briefly, in this graphical method V_T of

[^{11}C]3MeO4AP and V_T of [^{18}F]3F4AP are directly related to the specific binding ratio as shown in equation 1 below,

$$
V_T^{[^{11}C]3MeO4AP} = \frac{f_p^{[^{11}C]3MeO4AP}}{f_p^{[^{18}F]3F4AP}} \frac{K_D^{[^{18}F]3F4AP}}{K_D^{[^{11}C]3MeO4AP}} V_T^{[^{18}F]3F4AP}
$$
$$
+ V_{ND}^{[^{11}C]3MeO4AP}\left(1 - \frac{BP_{ND}^{[^{11}C]3MeO4AP}}{BP_{ND}^{[^{18}F]3F4AP}}\right)
$$

(1)

where $f_p^{[^{11}C]3MeO4AP}$ and $f_p^{[^{18}F]3F4AP}$ are the plasma free fractions, $K_D^{[^{11}C]3MeO4AP}$ and $K_D^{[^{18}F]3F4AP}$ are the equilibrium dissociation constants, $BP_{ND}^{[^{11}C]3MeO4AP}$ and $BP_{ND}^{[^{18}F]3F4AP}$ are the binding potentials (the ratio at equilibrium of specifically bound radioligand to that of nondisplaceable radioligand in tissue) for [^{11}C]3MeO4AP and [^{18}F]3F4AP, respectively and $V_{ND}^{[^{11}C]3MeO4AP}$ is the non-displaceable volumes of distribution of [^{11}C]3MeO4AP assumed to be homogeneous across brain regions. By plotting V_T of one tracer against V_T of the other tracer across several brain regions with different levels of binding, this graphical method allows: (1) to determine whether the two tracers bind to the same target (assessed by the linearity or lack of linearity of the regression), and (2) to identify which compound presents the higher signal-to-noise ratio (assessed from the sign of the y intercept). In addition, since measurements of $f_p^{[^{11}C]3MeO4AP}$ and $f_p^{[^{18}F]3F4AP}$ are available and both [^{11}C]3MeO4AP and [^{18}F]3F4AP enter the brain by passive diffusion, the slope of the linear regression provides information on the *in vivo* affinity ratio[18]. In each animal, the comparison was performed on the average V_T values of the radiotracers calculated from the two baseline scans. Regional [^{18}F]3F4AP V_T data were obtained from Guehl et al[16] (where Monkey 3 and 4 correspond, respectively, to Monkey 1 and 2 in the present work). Paired comparisons were plotted for the regional V_T estimates in occipital cortex, parietal cortex, temporal cortex, frontal cortex, hippocampus, amygdala, striatum, thalamus, white matter and whole cerebellum.

Statistical analysis: All data are expressed as mean value ± one standard deviation (SD). Agreement between methods or models was assessed by computing the average measured intraclass correlation coefficient (ICC) by use of a two-way mixed-effects model with absolute agreement definition. The Akaike Information Criterion (AIC) was used to assess the relative goodness of fit between compartment models.[19] AIC weights were computed to evaluate the probability of one model being preferred over the others.[31] The most statistically appropriate model is the one producing the smallest AIC values and highest AIC weights. The linear correlation between V_T of [^{11}C]3MeO4AP and V_T of [^{18}F]3F4AP (equation 1) was assessed using the Pearson's correlation coefficient r and the t distribution of the Fisher transformation was used to generate p values for linear regressions and intercept. A p value of 0.05 or less was considered statistically significant. Test-retest variability (TRT in %) of V_T estimates was calculated from the two baseline scans acquired

on the same day in Monkey 2 as $TRT(\%) = [(V_{T,baseline2} - V_{T,baseline1})/V_{T,baseline1}] \times 100$. The same equation was also used to calculate reproducibility of V_T measurements in Monkey 1 from the baseline scans that were acquired 3 months apart.

Supplementary Material

Refer to Web version on PubMed Central for supplementary material.

ACKNOWLEDGMENTS

References

1. Reich DS, Lucchinetti CF & Calabresi PA Multiple Sclerosis. N Engl J Med 378, 169–180, doi: 10.1056/NEJMra1401483 (2018). [PubMed: 29320652]

2. Aboul-Enein F et al. Preferential loss of myelin-associated glycoprotein reflects hypoxia-like white matter damage in stroke and inflammatory brain diseases. J Neuropathol Exp Neurol 62, 25–33 (2003). [PubMed: 12528815]

3. Bramlett HM & Dietrich WD Progressive damage after brain and spinal cord injury: pathomechanisms and treatment strategies. Prog Brain Res 161, 125–141, doi: 10.1016/S0079-6123(06)61009-1 (2007). [PubMed: 17618974]

4. Armstrong RC, Mierzwa AJ, Marion CM & Sullivan GM White matter involvement after TBI: Clues to axon and myelin repair capacity. Experimental neurology 275 Pt 3, 328–333, doi: 10.1016/j.expneurol.2015.02.011 (2016). [PubMed: 25697845]

5. Bronge L, Bogdanovic N & Wahlund LO Postmortem MRI and histopathology of white matter changes in Alzheimer brains. A quantitative, comparative study. Dement Geriatr Cogn Disord 13, 205–212, doi: 10.1159/000057698 (2002). [PubMed: 12006730]

6. Brugarolas P, Reich DS & Popko B Detecting Demyelination by PET: The Lesion as Imaging Target. Mol Imaging 17, 1536012118785471, doi: 10.1177/1536012118785471 (2018).

7. Bauckneht M et al. Molecular imaging of multiple sclerosis: from the clinical demand to novel radiotracers. EJNMMI Radiopharm Chem 4, 6, doi:10.1186/s41181-019-0058-3 (2019). [PubMed: 31659498]

8. Brugarolas P et al. Development of a PET radioligand for potassium channels to image CNS demyelination. Sci Rep 8, 607, doi: 10.1038/s41598-017-18747-3 (2018). [PubMed: 29330383]

9. Basuli F, Zhang X, Brugarolas P, Reich DS & Swenson RE An efficient new method for the synthesis of 3-[^{18}F]fluoro-4-aminopyridine via Yamada-Curtius rearrangement. J Labelled Comp Radiopharm 61, 112–117, doi: 10.1002/jlcr.3560 (2018). [PubMed: 28870001]

10. Brugarolas P, Freifelder R, Cheng SH & DeJesus O Synthesis of meta-substituted [^{18}F]3-fluoro-4-aminopyridine via direct radiofluorination of pyridine N-oxides. Chem Commun (Camb) 52, 7150–7152, doi: 10.1039/c6cc02362b (2016). [PubMed: 27216991]

11. Bagchi B et al. Disruption of myelin leads to ectopic expression of $K_V1.1$ channels with abnormal conductivity of optic nerve axons in a cuprizone-induced model of demyelination. PLoS One 9, e87736, doi: 10.1371/journal.pone.0087736 (2014). [PubMed: 24498366]

12. Sinha K, Karimi-Abdolrezaee S, Velumian AA & Fehlings MG Functional changes in genetically dysmyelinated spinal cord axons of shiverer mice: role of juxtaparanodal Kv1 family K^+ channels. Journal of neurophysiology 95, 1683–1695, doi:10.1152/jn.00899.2005 (2006). [PubMed: 16319208]

13. Arroyo EJ, Sirkowski EE, Chitale R & Scherer SS Acute demyelination disrupts the molecular organization of peripheral nervous system nodes. The Journal of comparative neurology 479, 424–434, doi :10.1002/cne.20321 (2004). [PubMed: 15514980]

14. Karimi-Abdolrezaee S, Eftekharpour E & Fehlings MG Temporal and spatial patterns of $K_v1.1$ and $K_v1.2$ protein and gene expression in spinal cord white matter after acute and chronic spinal cord injury in rats: implications for axonal pathophysiology after neurotrauma. The European journal of neuroscience 19, 577–589 (2004). [PubMed: 14984408]

15. Rasband MN et al. Potassium channel distribution, clustering, and function in remyelinating rat axons. The Journal of neuroscience: the official journal of the Society for Neuroscience 18, 36–47 (1998). [PubMed: 9412484]

16. Guehl NJ et al. Evaluation of the potassium channel tracer [^{18}F]3F4AP in rhesus macaques. J Cereb Blood Flow Metab, 271678X20963404, doi:10.1177/0271678X20963404 (2020).

17. Rodriguez-Rangel S, Bravin AD, Ramos-Torres KM, Brugarolas P & Sanchez-Rodriguez JE Structure-activity relationship studies of four novel 4-aminopyridine K^+ channel blockers. Sci Rep 10, 52, doi: 10.1038/s41598-019-56245-w (2020). [PubMed: 31919372]

18. Guo Q, Owen DR, Rabiner EA, Turkheimer FE & Gunn RN A graphical method to compare the in vivo binding potential of PET radioligands in the absence of a reference region: application to [^{11}C]PBR28 and [^{18}F]PBR111 for TSPO imaging. J Cereb Blood Flow Metab 34, 1162–1168, doi: 10.1038/jcbfm.2014.65 (2014). [PubMed: 24736889]

19. Akaike H A new look at the statistical model identification. IEEE Transactions on Automatic Control 19, 716–723, doi: 10.1109/TAC.1974.1100705 (1974).

20. King AM, Menke NB, Katz KD & Pizon AF 4-aminopyridine toxicity: a case report and review of the literature. Journal of medical toxicology: official journal of the American College of Medical Toxicology 8, 314–321, doi: 10.1007/s13181-012-0248-9 (2012). [PubMed: 22782458]

21. Seidlitz J et al. A population MRI brain template and analysis tools for the macaque. NeuroImage 170, 121–131, doi: 10.1016/j.neuroimage.2017.04.063 (2018). [PubMed: 28461058]

22. Filippi M & Rocca MA MR imaging of multiple sclerosis. Radiology 259, 659–681, doi: 10.1148/radiol.11101362 (2011). [PubMed: 21602503]

23. Tomassy GS et al. Distinct profiles of myelin distribution along single axons of pyramidal neurons in the neocortex. Science 344, 319–324, doi: 10.1126/science.1249766 (2014). [PubMed: 24744380]

24. Fox RJ, Beall E, Bhattacharyya P, Chen JT & Sakaie K Advanced MRI in multiple sclerosis: current status and future challenges. Neurol Clin 29, 357–380, doi: 10.1016/j.ncl.2010.12.011 (2011). [PubMed: 21439446]

25. Coman I et al. Nodal, paranodal and juxtaparanodal axonal proteins during demyelination and remyelination in multiple sclerosis. Brain: a journal of neurology 129, 3186–3195, doi: 10.1093/brain/awl144 (2006). [PubMed: 16766541]

26. Collier T, Normandin M, El Fakhri G & Vasdev N Automation of column-switching HPLC for analysis of radiopharmaceuticals and their metabolites in plasma. Society of Nuclear Medicine Annual Meeting Abstracts 54, 1133 (2013).

27. Hilton J et al. Column-switching HPLC for the analysis of plasma in PET imaging studies. Nucl Med Biol 27, 627–630, doi: 10.1016/s0969-8051(00)00125-6 (2000). [PubMed: 11056380]

28. Innis RB et al. Consensus nomenclature for in vivo imaging of reversibly binding radioligands. J Cereb Blood Flow Metab 27, 1533–1539, doi: 10.1038/sj.jcbfm.9600493 (2007). [PubMed: 17519979]

29. Logan J et al. Graphical analysis of reversible radioligand binding from time-activity measurements applied to [N-^{11}C-methyl]-(−)-cocaine PET studies in human subjects. J Cereb Blood Flow Metab 10, 740–747, doi: 10.1038/jcbfm.1990.127 (1990). [PubMed: 2384545]

30. Ichise M, Toyama H, Innis RB & Carson RE Strategies to improve neuroreceptor parameter estimation by linear regression analysis. J Cereb Blood Flow Metab 22, 1271–1281, doi: 10.1097/01.WCB.0000038000.34930.4E (2002). [PubMed: 12368666]

31. Burnham KP & Burnham KP Model selection and multi-model inference: a practical information-theoretic approach. 2nd edn, (Springer, 2002).
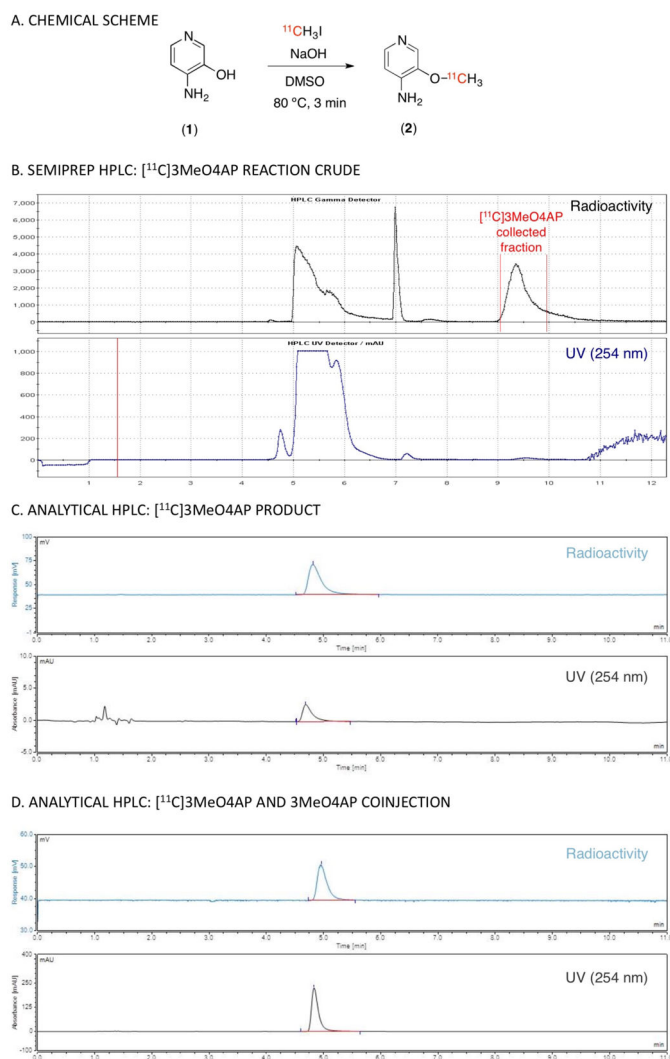
A. CHEMICAL SCHEME

B. SEMIPREP HPLC: [¹¹C]3MeO4AP REACTION CRUDE

C. ANALYTICAL HPLC: [¹¹C]3MeO4AP PRODUCT

D. ANALYTICAL HPLC: [¹¹C]3MeO4AP AND 3MeO4AP COINJECTION

Figure 1. Radiochemical synthesis of 3-[¹¹C]methoxy-4-aminopyridine.
(**A**) Chemical reaction scheme. (**B**) Semiprep HPLC purification (radio and UV chromatograms). (**C**) Analytical HPLC (radio and UV chromatograms) of tracer only. (**D**) Analytical HPLC (radio and UV chromatograms) of tracer plus reference standard.
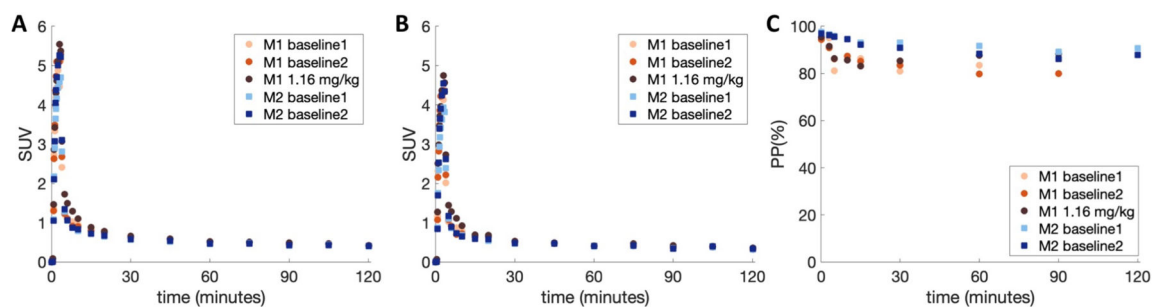
Figure 2: [11C]3MeO4AP in arterial blood.
(**A**) Time course in whole blood (WB). (**B**) Time course in plasma (PL). (**C**) [11C]3MeO4AP percent parent in plasma (%PP). In the legends, M1 and M2 refer to Monkey 1 and 2, respectively.
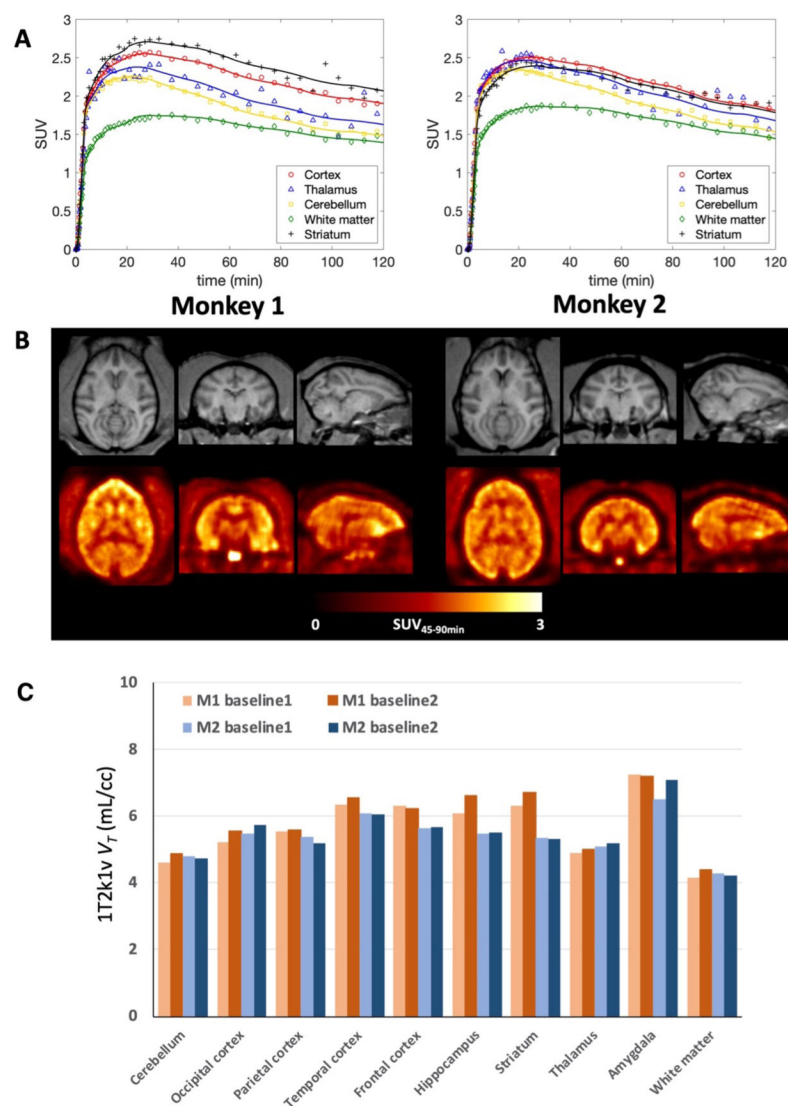
Figure 3: [^{11}C]3MeO4AP in the primate brain.
(**A**) Brain time activity curves and model fits using a reversible 1T model with the vascular contribution v included as a model parameter (1T2k1v). (**B**) Individual MRI MEMPRAGE (top) and PET SUV images calculated from 45 to 90 min post tracer injection (SUV$_{45\text{-}90\text{min}}$) (bottom). Images are presented in the MRI NIMH Macaque template (NMT) space[21]. For each panel (A and B), left corresponds to data acquired in Monkey 1 and right corresponds to Monkey 2. For each monkey, data shown correspond to a single baseline study. (**C**) Regional V_T values for each baseline scan and animal.
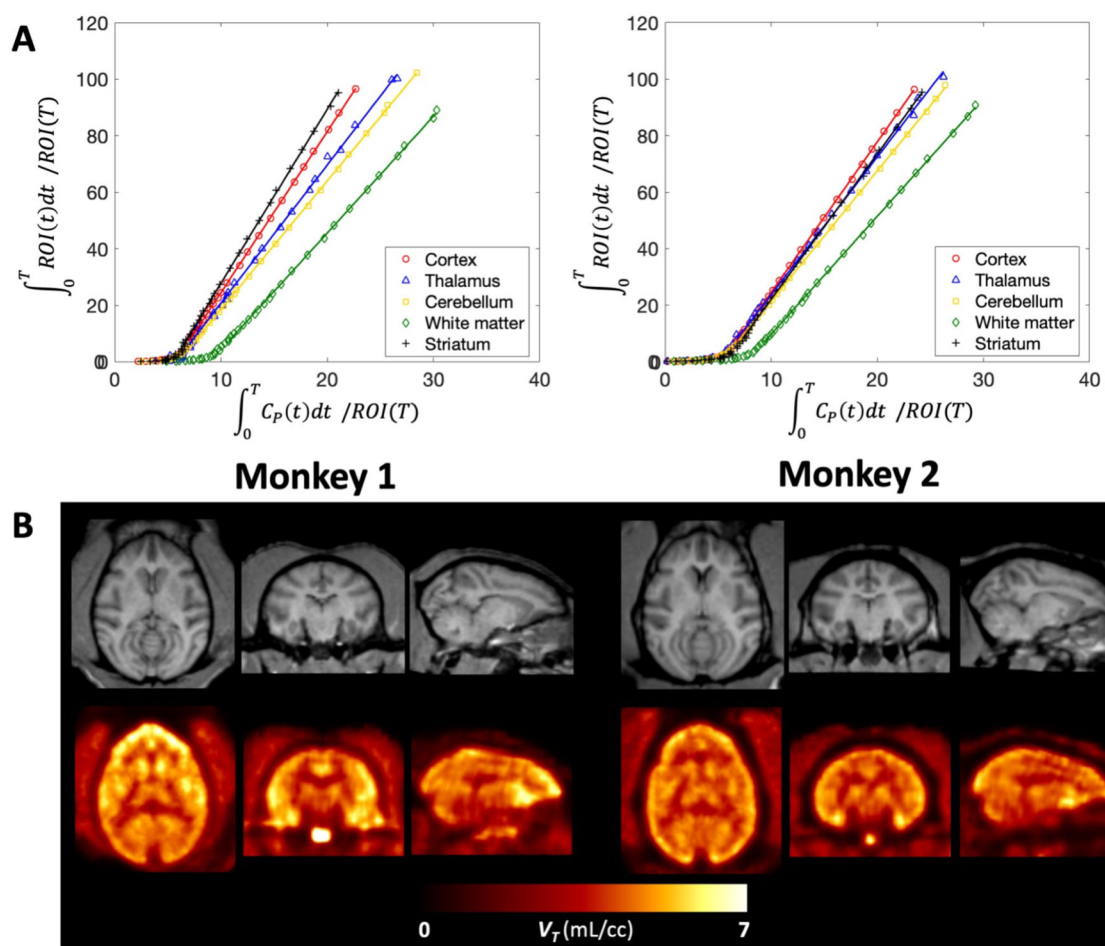
Figure 4: Graphical analysis of [^{11}C]3MeO4AP in the primate brain.
(**A**) Logan plots using a 10-min t^*. (**B**) Individual MRI MEMPRAGE images (top) and PET parametric images of total volume of distribution V_T (bottom), after registration into the NMT space. For each panel (A and B), left corresponds to data acquired in Monkey 1 and right corresponds to Monkey 2. For each monkey, data shown correspond to a single baseline study. Logan plots (A) and Logan V_T parametric maps were generated using 90 minutes of data.
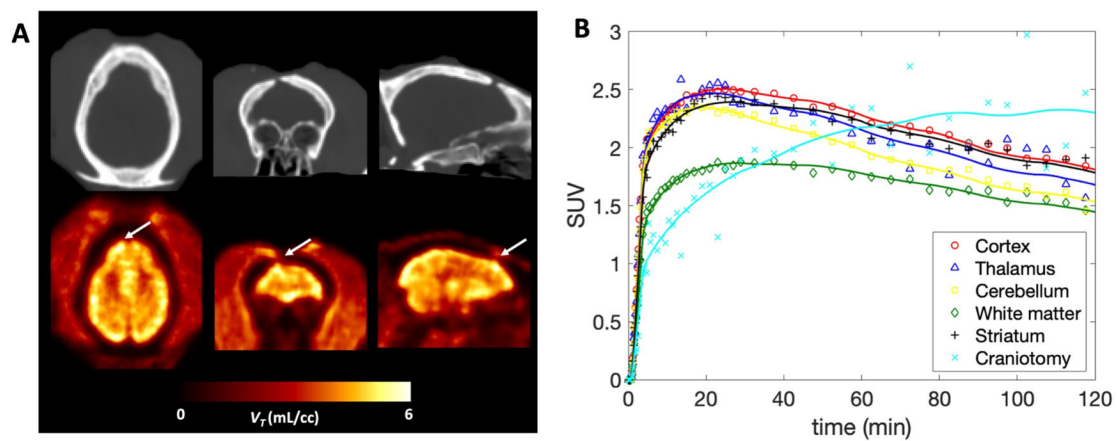
Figure 5: [^{11}C]3MeO4AP in the focal brain injury.
(**A**) CT and [^{11}C]3MeO4AP parametric images of V_T with axial, coronal and sagittal view showing the injury. Arrows indicate the location of the lesion. (**B**) Time activity curves including the lesion in light blue of Monkey 2 showing distinct kinetics compared to other regions.
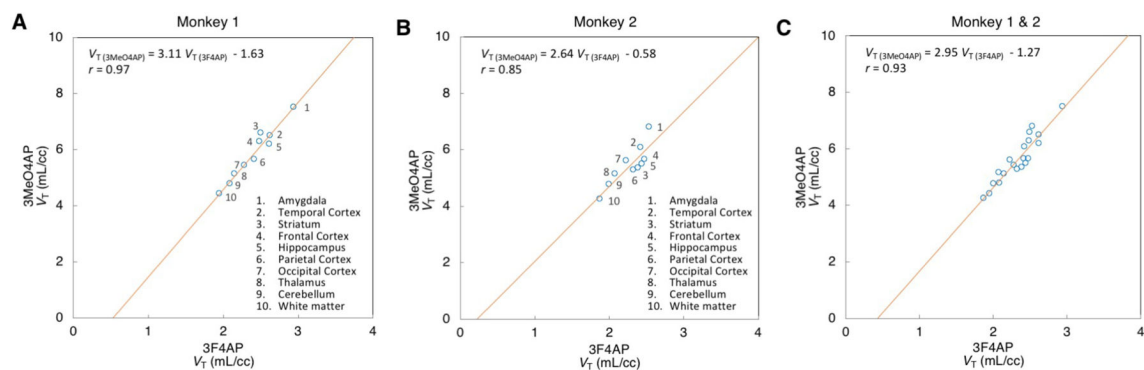
Figure 6: Scatter plots comparing the V_T values obtained for [^{11}C]MeO4AP and [^{18}F]3F4AP in Monkey 1 (A), Monkey 2 (B) and both together (C).

For each radiotracer the plotted V_T values represent the average of the two baseline scans.

Paired comparisons are plotted for the regional V_T estimates in occipital cortex, parietal cortex, temporal cortex, frontal cortex, hippocampus, amygdala, striatum, thalamus, white matter and whole cerebellum. Red lines represent the linear regression lines.

Table 1:

Regional 1T2k1v V_T estimates obtained from all studies

ROI	Monkey 1			Monkey 2	
	Baseline 1	**Baseline 2**	**1.16 mg/kg**	**Baseline 1**	**Baseline 2**
Cerebellum	4.59	4.89	4.55	4.79	4.74
Occipital Cortex	5.21	5.55	5.21	5.47	5.74
Parietal Cortex	5.53	5.59	5.40	5.37	5.18
Temporal Cortex	6.35	6.54	6.47	6.09	6.06
Frontal Cortex	6.30	6.23	6.40	5.63	5.66
Hippocampus	6.07	6.60	6.13	5.47	5.51
Striatum	6.30	6.71	6.51	5.36	5.32
Thalamus	4.90	5.02	4.99	5.09	5.19
Amygdala	7.23	7.20	7.00	6.50	7.08
White matter	4.17	4.40	4.21	4.27	4.21
Whole brain	5.16	5.40	5.19	4.99	5.02